Water-gas shift: Characterization and testing of nanoscale YSZ supported Pt catalysts

Michela Martinelli [a,b], Gary Jacobs [a], Uschi M. Graham [a], Wilson D. Shafer [a], Donald C. Cronauer [c], A. Jeremy Kropf [c], Christopher L. Marshall [c], Syed Khalid [d], Carlo G. Visconti [b], Luca Lietti [b], Burtron H. Davis [a,*]

[a] *Center for Applied Energy Research, University of Kentucky, 2540 Research Park Dr., Lexington, KY 40511, USA*
[b] *Politecnico di Milano, Dipartimento di Energia, Piazza Leonardo da Vinci, Milano 20133, Italy*
[c] *Argonne National Laboratory, Argonne, IL 60439, USA*
[d] *National Synchrotron Light Source, Brookhaven National Laboratory, Brookhaven Ave, Upton, NY 11973, USA*

Received 23 October 2014
Received in revised form
25 November 2014
Accepted 2 December 2014
Available online 14 March 2015

1. Introduction

Interest in water-gas-shift (WGS) has increased in recent decades due to advances in PEM fuel cell technology for portable power and transportation applications [1,2]. Conventional $Cu/ZnO/Al_2O_3$ catalysts used commercially for low temperature shift are pyrophoric and unamenable to the rapid start-up/shutdown steps occurring in a fuel processor for fuel cell applications. Thus, a non-pyrophoric WGS catalyst with high activity at low temperature is needed. One family of catalysts that is promising for the development of the low temperature WGS stage is comprised of a metal catalyst (e.g., Pt) deposited on a partially reducible oxide (PRO) (e.g. ceria, zirconia, etc.). The metallic center is suggested to play the dual role of facilitating the partial reduction of the support as well as participating in the mechanism [3,4].

Two primary mechanisms have been proposed for WGS. In the redox mechanism [4–6], which has found support from isotopic tracer studies [6], CO adsorbed on the precious metal is proposed to react with O-adatoms on the PRO to generate CO_2, leaving oxygen vacancies in the surface of the support. Oxygen vacancies are replenished by reduction of H_2O, yielding H_2.

Kinetic isotope effect, isotopic tracer, and operando studies suggest that associative mechanisms involve adsorbed surface intermediates such as formates [7–12], and carboxylates [12–16]. The precious metal facilitates the formation of defect sites in the PRO. H_2O dissociates at these defects to generate Type II OH groups, which in turn react with CO to form associated species (e.g., formates and/or carboxylates). In the presence of co-adsorbed H_2O, formate has been identified to decompose in the forward direction to H_2 and adsorbed an adsorbed CO_2 species, which decomposes.

In either mechanism, the surface shell of the support undergoes reduction and provides surface oxygen mobility. In the redox mechanism, this is important for removing O adatoms by reaction with CO. In associative mechanisms, adsorbed intermediates are

* Corresponding author. Tel.: +1 859 257 0251; fax: +1 859 257 0302.
E-mail address: burtron.davis@uky.edu (B.H. Davis).

bound by their O atoms. Transport to the metal-support interface is important for forward decomposition.

Among the PRO supports, CeO_2 is the most studied because of its high catalytic activity [17,18]; however, in many cases, it has been found to rapidly deactivate with the time on stream [4,19]. Loss of active metal surface, irreversible "over"-reduction of ceria by H_2 or the formation of stable carbonates on the surface have been proposed as causes of the deactivation of Pt/CeO_2. On the contrary, Pt/ZrO_2 catalysts have been reported to exhibit much better stability as a consequence of the acidity of the support; that is, carbonates are less stable on the surface [20]. Moreover, zirconia is 2.5 times more abundant than ceria and is produced worldwide. For catalytic applications, replacements for rare earth elements are of interest, due to their more limited or controlled supply.

On the other hand, Pt/ZrO_2 catalysts have been found to exhibit lower activity in the range of low temperature WGS compared to ceria-based supports [21]. Chenu et al. [22] found that Pt/ZrO_2 catalysts exhibited lower formate band intensities upon adsorption of CO to the activated catalyst in relation to Pt/ceria, and suggested a lower density of defect-associated bridging OH groups (as defined by Binet et al. [23] for partially reduced ceria).

To increase activity, promoters have been added to Pt/ZrO_2. To date, few investigations have been reported [20,24–30]. Iida and Igarashi [24,25] found enhanced activity by promoting Pt/ZrO_2 with Re to form a bimetallic catalyst. The authors observed that the formate species during WGS were more reactive (lower coverage in IR) over promoted catalysts. They concluded that Re imparts a redox cycle during the formation of the active OH group. This was suggested to accelerate the turnover rate of formate species, with Pt—CO providing sites for associating with Re—OH groups in order to form the bidentate formate species.

In 2005, Brooks at al. [26] reported an improvement in catalytic activity when Pt/ZrO_2 was doped with Group 1 elements (Li, Na or K), with Na yielding the greatest enhancement. In 2007, Pigos et al. [27,28] reported results of DRIFTS spectroscopy demonstrating that the formate species were more reactive on the Na-promoted catalyst relative to Pt/ZrO_2 alone. A shift to lower wavenumbers of the formate C H-band indicated bond weaken-ing, the breaking of which Shido and Iwasawa [7] identified as being the rate limiting step for related Rh/ceria catalysts. Three separate tests were conducted [27,28], including (I) steady state CO adsorption and WGS experiments at 225 °C; (II) transient formate decomposition studies at 130 °C; and (III) formate decomposition test under dry conditions using hydrogen–deuterium exchange at 225 °C.

Hwang et al. [20] indicated that the addition of titanium enhances the WGS reaction rate by a factor of about 3 relative to Pt/ZrO_2 alone. Titanium addition increased the dispersion of Pt and the reducibility of $Pt/Ti/ZrO_2$ system, resulting in an increased density of surface hydroxyl groups. Formate species located close to the metal particles decomposed faster than those positioned remotely, with the involvement of a multi-coordinate OH group.

Addition of Group 5 elements has been explored. Nguyen-Thanh et al. [29] found that higher activities occur at lower vanadia loadings, and at this level the monovanadate species is the predominant one. Vanadia doping improved the reducibility of the support, so that the oxygen vacancies and OH groups would form more easily. Niobium addition was studied by Goscianska et al. [30]; the authors found that an enhancement in catalytic performance can only be obtained at low niobium loadings (optimal value of 0.3).

Computer models have revealed that divalent (e.g., Ca, Mn, Ni and Zn) [31], trivalent (e.g., Sc, Mn, Y, Gd and La) [32] and isovalent (e.g., Zr, Hf, Th) [33,34] dopants lower the reduction energy of CeO_2 up to a defect concentration of 50%. Oxygen vacancies generated by acceptor dopants allow the cell to more easily accommodate the strain caused by forming the larger Ce^{3+} species. The higher concentration of vacancies due to dopant addition increases O-mobility. Computational results have been confirmed by experimental results [35,36]. By incorporating Ca into the ceria lattice, Linganiso et al. [36] observed an improvement in surface O-mobility by following transient forward formate decomposition in a low concentration of steam. Higher WGS rates were observed with increases in Ca doping.

In principle, similar results might be obtained by doping zirconia with an appropriate element. When Zr^{4+} cations are substituted by Y^{3+} cations, oxygen vacancies are formed to maintain charge neutrality [37,38]. Yttrium stabilized zirconia (YSZ) has been the subject of intense research as a solid electrolyte for fuel cells [38]. However, few studies have focused on the surface O mobility property of YSZ, or the greater surface defect densities of YSZ for WGS. Silver et al. [39] used YSZ to improve the catalytic activity for CO hydrogenation. The authors found that the active sites for hydrogenation include vacancies, and that the reaction rate is enhanced because the mobility of oxygen is increased. Recently, computational studies have revealed that addition of yttria results in a decrease in the Zr^{4+}/Zr^{3+} reduction energy, which is more pronounced at higher dopant concentrations [40]. In one investigation utilizing a low surface area YSZ support for Pt particles, the catalyst exhibited catalytic activity that was higher than when non-reducible supports (e.g., Al_2O_3 and SiO_2) were used, but not as high as when ceria was employed [41]. Pt/YSZ catalysts [42] have also been explored for the electrochemical promotion of catalysis (EPOC) effect [43], where O_2^- pumping measurements (to and from the catalyst surface) led to changes in water-gas shift rates (nega-tive and positive, respectively). The positive increase in the rate was proposed to be due to a weakening of the Pt CO bond strength as well as an increase in surface oxygen vacancies, the latter of which
facilitated H_2O dissociation to generate active OH groups for the mechanism.

The aim of the current study is to explore YSZ for WGS by investigating the effect of yttrium addition on structure, reducibility and oxygen mobility, and to correlate these properties with catalytic activity.

2. Experimental

2.1. Catalyst preparation

High surface area mixed oxides were prepared by homogeneous precipitation of zirconia and yttrium nitrate, using sodium hydrox-ide (Fisher-Scientific) as the precipitating agent. In this method, appropriate amounts of $ZrO(NO_3)_2{\cdot}xH_2O$ (Alfa Aesar, 99.9%) and $Y(NO_3)_3{\cdot}6H_2O$ (Alfa Aesar, 99.9%) were dissolved simultaneously in deionized water at room temperature. The total ion concentra-tion was maintained at the 0.25 M level for all experiments. The prepared solution was added drop-wise to the sodium hydrox-ide solution (1 M), accompanied by constant stirring at 800 rpm to avoid the formation of lumps and to ensure complete dissolu-tion. The resulting precipitate was filtered and then washed several times until the filtered water had a pH of 7. The solid obtained was dried in a static oven at 110 °C overnight. The dried material was crushed and then calcined at 400 °C for 4 h. The support obtained was promoted with platinum via incipient wetness impregna-tion by taking into consideration the pore volume measured by
N_2 physisorption. An appropriate amount of $Pt(NH_3)_4(NO_3)_2$ (Alfa Aesar, 99.99%) was dissolved in water and the solution was added drop-wise in order to obtain 0.5% by weight Pt. The resulting material was dried at 110 °C overnight and then calcined at 350 °C for 4 h. Before catalytic testing, the samples were sieved in the diameter range of 63 μm < ϕ < 106 μm.

2.2. BET surface area and porosity

BET surface area was determined using a Micromeritics TRISTAR 3000 gas adsorption analyzer. In each test, approximately 300 mg of sample was used. The adsorption gas was nitrogen and the analysis was performed at the boiling temperature of liquid nitrogen. Samples were degased under vacuum for 12 h at 160 °C before conducting the nitrogen adsorption measurements. The specific surface areas were determined by the Brunauer–Emmett–Teller (BET) method.

2.3. X-ray diffraction

Diffraction patterns on calcined promoted support materials were recorded using a Philips X'Pert diffractometer. Short scan times were used over a long range to observe the changes, if any, in the crystal structure of YSZ relative to undoped zirconia. The conditions were as follows: scan rate of 0.008° per step, scan time of 60 s per step over a 2θ range of 15–90°. Long scan times were also employed over a short range in order to estimate the domain size by line broadening analysis. The conditions employed were a scan rate of 0.017° per step, a scan time of 150 s per step, and 2θ range of 20–40°.

2.4. Temperature programmed reduction

Temperature programmed reduction (TPR) was carried out on undoped zirconia, yttrium doped zirconia supports, as well as unpromoted and platinum promoted catalysts, using a Zeton-Altamira AMI-200 unit, equipped with a thermal conductivity detector (TCD). Argon was used as the reference gas, and 10% H_2 (balance argon) was flowed at 30 ml/min as the temperature was increased from 50 to 1100 °C at a heating rate of 10 °C/min. The thermocouple was situated inside the catalyst bed, and approximately 300 mg of sample were used for each experiment.

2.5. X-ray absorption near edge and extended X-ray absorption fine structure spectroscopies (XANES/EXAFS)

In situ H_2-TPR studies were performed at the Materials Research Collaborative Access Team (MR-CAT) beamline at the Advanced Photon Source, Argonne National Laboratory. A cryogenically cooled Si (1 1 1) monochromator selected the incident energy and a rhodium-coated mirror rejected higher order harmonics of the fundamental beam energy. The experiment set up was similar to that outlined by Jacoby [44]. A stainless steel multi-sample holder (4.0 mm i.d. channels) was used to monitor the in situ reduction of 6 samples during a single TPR run. The holder was placed in the center of a quartz tube, equipped with gas and thermocouple ports and Kapton windows. The amount of sample was optimized for Y (17,047 eV) and Zr (18,008 eV) K-edge and for Pt L_{III}-edge (11,566 eV). The quartz tube was placed in a clamshell furnace mounted on a positioning table. Each sample cell was positioned relative to the beam by finely adjusting the position of the table to an accuracy of 20 μm (for repeat scans). Once the sample positions were fined-tuned, the reactor was purged with helium for more than 5 min at 30 ml/min. Then, the reactant gas (H_2/He, 4%) was flowed through the sample (30 ml/min) and a temperature ramp (of 3 °C/min for Y and Zr K-edges and 1.2 °C/min for Pt L_{III} edge) was initiated for the furnace to achieve the desired temperature (>800 °C for Y and Zr edges, and ~500 °C for Pt L_{III} edge). After the temperature ramp, the samples were cooled to ambient temperature and scanned. The Y, Zr and Pt spectra were recorded in transmission mode and the respective metallic foil (in the cases of Zr and Pt) was measured simultaneously with each sample spectrum for energy calibration. X-ray absorption spectra for each sample were collected from 17,900 to 18,170 eV for the Zr K-edge, from 16,920 to 17,200 eV for the Y K-edge and from 11,360 to 12,110 eV for the Pt L_{III} edge.

Data reduction of EXAFS/XANES spectra was carried out by using the WinXAS program [45], and raw data were processed to give the normalized XANES spectra. Linear combination fitting of platinum spectra with appropriate reference compounds was carried out.

2.6. High resolution transmission electron microscopy

Catalyst powders were collected on copper grids for TEM analysis (200-mesh, Ted Pella Inc. Redding, CA). TEM imaging was performed using a JEOL 2010F field-emission gun transmission electron microscope (accelerating voltage of 200 keV and magnification ranging from 50 to 1000 K). A symmetrical multi-beam illumination was used for high-resolution imaging (HRTEM) with a beam resolution of 0.5 nm. Images were recorded with a Gatan Ultrascan 4k × 4k CCD camera. All data processing and analysis was performed using Gatan Digital Micrograph software. Scanning transmission electron microscopy (STEM) was conducted with a high angle annular dark field (HAADF) detector and Gatan imaging filter (GIF).

2.7. Diffuse reflectance Fourier transform infrared spectroscopy

A Nicolet Nexus 870 infrared spectrometer was used equipped with a DTGS-TEC detector. A chamber fitted with ZnSe windows was utilized as the WGS reactor for in situ measurements. Experimental procedures are provided elsewhere [46]. For each run, the catalyst was first activated at 350 °C in 160 ml/min of 68% H_2 (balance He) for 2 h and then cooled down to 225 °C. Formates were generated using the following procedure. To achieve the Type II bridging OH group on the surface a mixture of 38.9 ml/h of H_2O and H_2 was fed to the sample at 225 °C, and after that the feed was switched to a mixture consisting of 33.8 ml/min of 10% CO/He and 66.1 ml/min He. When H_2O is completely removed from the system, formate generated from reaction of type II bridging OH groups and CO cannot undergo forward decomposition to hydrogen and unidentate carbonate, the latter being the precursor to CO_2 formation. After the formate was generated, the temperature was lowered to 130 °C and the catalyst was exposed to 2.8% (vol.%) H_2O vapor generated from a bubbler using helium for 15 min. The total flow rate during formate decomposition was 20 ml/min. After the decomposition of the formate, the system was purged with 66 ml/min of helium.

2.8. Water-gas-shift reaction

The catalytic tests of LT-WGS were carried out in a stainless fixed bed tubular reactor (0.444 in. i.d.) under steady state conditions. In a typical run 720 mg of catalyst (63–106 μm in size) diluted with 1280 mg glass beads (60–80 μm in size) were packed between two layers of quartz wool. Using the glass beads minimized the effect of heat generated by the mildly exothermic reaction. Note that prior to selection of the sieve range, measurements were conducted over different sieve ranges, moving from larger to smaller particle size ranges, to rule out mass transport resistances and channeling effects. The temperature of the catalyst bed was monitored by a K-type thermocouple and maintained by a temperature controller (Barber Colman). Prior to testing, the catalysts were first reduced in H_2 (100 ml/min) at 350 °C for 1 h (ramp rate of 4 °C/min). Then, a gas mixture containing 3.0% CO, 26.1% H_2O, 29.9% H_2, 5% N_2 (balance He) was used for the catalytic tests to mimic, except for the case of CO_2, LTS conditions found in a typical processor for fuel cell applications. The dry gases were controlled using Brooks mass flow controllers. Steam was provided to the system via a steam

Table 1
BET surface area and porosity measurements from physisorption of nitrogen at 77 K, including supports and the corresponding Pt-promoted catalysts.

Catalyst description	BET SA [m^2/g]	Average pore volume [cm^3/g]	Average pore radius [nm]
ZrO_2	103	0.15	3.0
0.5%Pt/ZrO_2	108	0.15	2.9
$Zr_{0.9}Y_{0.1}O_{1.95}$	162	0.16	1.9
0.5%Pt/$Zr_{0.9}Y_{0.1}O_{1.95}$	153	0.16	2.1
$Zr_{0.75}Y_{0.25}O_{1.875}$	183	0.15	1.5
0.5%Pt/$Zr_{0.75}Y_{0.25}O_{1.875}$	174	0.14	1.5
$Zr_{0.5}Y_{0.5}O_{1.75}$	186/191	0.13	1.6
0.5%Pt/$Zr_{0.5}Y_{0.5}O_{1.75}$	172	0.12	1.6
$Zr_{0.25}Y_{0.75}O_{1.625}$	189	0.15	1.6
0.5%Pt/$Zr_{0.25}Y_{0.75}O_{1.625}$	159	0.13	1.6
$Zr_{0.1}Y_{0.9}O_{1.55}$	162	0.18	1.7
0.5%Pt/$Zr_{0.1}Y_{0.9}O_{1.55}$	124	0.14	1.8
Y_2O_3	151	0.31	3.0
0.5%Pt/Y_2O_3	110	0.25	3.3

Table 2
Domain size as determined by line broadening analysis using the integral breadth method.

Catalyst	2-θ	Size [nm]
Pt/ZrO_2	30.31	7.9
	50.54	7.0
0.5%Pt/$Zr_{0.9}Y_{0.1}O_{1.95}$	30.29	6.5
	50.47	5.6
0.5%Pt/$Zr_{0.75}Y_{0.25}O_{1.875}$	30.21	3.0
	50.28	3.1
0.5%Pt/$Zr_{0.5}Y_{0.5}O_{1.75}$	29.89	1.3
	49.76	1.9
0.5%Pt/$Zr_{0.25}Y_{0.75}O_{1.625}$	30.16	1.2
	49.25	1.9
0.5%Pt/$Zr_{0.1}Y_{0.9}O_{1.55}$	29.59	1.3
	48.92	2.2
0.5%Pt/Y_2O_3	29.99	1.4
	48.17	1.3

generator consisting of a hollow cylinder (50 mm i.d., 150 mm long) packed with quartz wool. Water was fed by infusion with a syringe pump (Thermo Scientific, Model Orion M361) into the steam generator via a 1/16 in. needle with a side-port hole. The entire system was heated to 200 °C to avoid condensation of water. The feed was adjusted in bypass mode to obtain a steady state concentration of $CO/H_2O/N_2$/He prior to bringing the catalyst on-line (concentration = 3.0/26.1/5/29.9/36 mol%, where N_2 was used as an internal standard). The GHSV during the reaction test was 120,220 h^{-1}. The products were passed through a cold trap cooled to 0 °C to condense water from the gas prior to GC analysis. The SRI 8610 GC includes two columns (3.658 m silica gel packed and 1.829 m molecular sieve packed) and two detectors (FID and TCD). To boost the sensitivity of the CO and CO_2 signals, the GC incorporates a methanizer, such that these products can be analyzed by FID.

3. Results and discussion

3.1. BET surface area and porosity

In Table 1 the BET results are reported for the supports and for the corresponding Pt-promoted catalysts. The surface areas for the un-promoted supports reach a maximum at a Y/Zr ratio of 1:1 (191 m^2/g). The average pore size for the unpromoted catalysts decreases by increasing the yttrium until a minimum value of 1.5 nm for the system $Zr_{0.75}Y_{0.25}O_{1.875}$. The average pore volume does not significantly change among the different systems, the only exception being the Y_2O_3 support which exhibited a higher aver-age pore volume (0.31 cm^3/g). When platinum is added the surface area did not change significantly for the ZrO_2 catalyst, while a significant decrease was observed for all of the doped supports and in the case of Y_2O_3; this is associated with an increase in the aver-age pore radius and is likely due to some pore blocking, especially in the case of the narrower pores. Another possibility is that the doped zirconia samples may be more unstable than the ZrO_2 such that platinum impregnation could alter the morphology of the catalyst. Indeed, the loss of surface area was more pronounced at higher yttrium loadings (i.e., the fractional loss in area increases from 5.1%for 0.5%Pt/$Zr_{0.9}Y_{0.1}O_{1.95}$ to 27.5% for 0.5% Pt/Y_2O_3).

3.2. Catalyst structure: XRD/XANES/HR-TEM

Fig. 1 shows the XRD patterns for the Pt-promoted samples. The patterns for the zirconia catalyst display peaks that could correspond to either the cubic or to the tetragonal phase. The assignment of cubic or tetragonal phase based on X-ray diffraction analysis, can be misleading because the structures of the two phases are very similar. Srivastava at al. [47] reported that the tetragonal structure can be distinguished from the cubic structure by the presence of characteristic splitting of the tetragonal phase, [e.g., (0 0 2) (2 0 0), (1 1 3) (3 1 1), (0 0 4) (4 0 0), and (0 0 6) (6 0 0)], whereas the cubic phase exhibits only single peaks at all of these positions. For the sample prepared by precipitation, the doublets indicative of the tetragonal phase at intermediate 2θ positions are difficult to distinguish clearly because of peak broadening due to small crystallite sizes. Davis [48] and Srinivasan et al. [49] have suggested that the crystal structure obtained at low pH values and high pH values is tetragonal. The ZrO_2 sample in this work was precipitated at a pH of 12 and exhibits the tetragonal phase.

The XANES spectrum for the oxidized sample can also be used to determine if the structure is either tetragonal or cubic. In Fig. 2 (left), the XANES spectrum for the Pt/ZrO_2 catalyst is reported. A number of features in the lineshape suggest that the structure is tetragonal. For example, a small shoulder exists at about at 6–7 eV beyond the Zr K-edge threshold, which is most apparent in tetragonal zirconia [50]. In general, XANES features within 10 eV of the edge threshold are due to electronic transition to unoccupied high-energy states near the Fermi level and are sensitive to the local geometry of the absorbing atom. So, the shoulder can be attributed to a 1s 4d transition, which is forbidden unless some d–p mixing occurs. The intensity of this transition is stronger in compounds that are distorted from the case of centrosymmetry [51,52]. Since tetragonal geometries are known to enhance d–p coordination relative to that seen for seven fold coordination (due to the lack of centrosymmetry), the stronger transition in t-ZrO_2 is understandable. Secondly, the spectrum has a prominent shoulder at 18.037 keV that is not present in other zirconia phases. This peak corresponds to multiple scattering involving second nearest neighbor atoms or higher shells.

By increasing the yttrium loading the intensity of the XRD peaks in Fig. 1 gradually decrease, indicating a lower degree of crystallinity. This suggests that crystallization occurs at higher temperatures for the Y-doped catalysts. Line broadening analysis using the integral breadth method suggests that the oxide (mixed oxide) domain size decreased with Y-doping and became less crystalline, and that the average domain size was 7.9 nm for 0.5%Pt/ZrO_2 and ~1.3 nm for 0.5%Pt/Y_2O_3 (Table 2). The estimates neglect the possible influence of microstrain on peak broadening, as an attempt at employing the Hall–Williamson method proved inconclusive.

Regarding the mixed oxides, the XRD signal was not significantly broadened only for the sample with a composition of 0.5%Pt/$Zr_{0.9}Y_{0.1}O_{1.95}$. In this case, the peaks appear to correspond to a tetragonal structure. In the literature, it is reported that a small amount of Y (less than 16 mol%) stabilizes the tetragonal

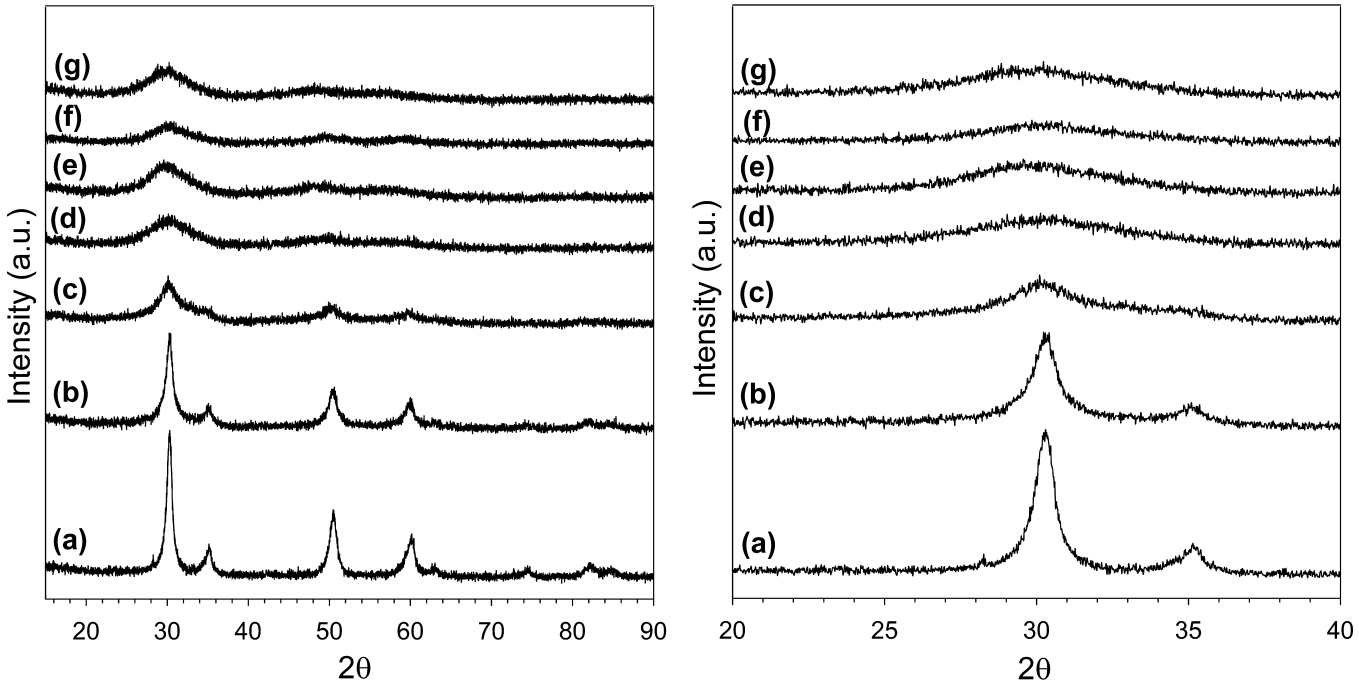

Fig. 1. X-ray diffraction profiles at (left) short scan times over a long range and (right) long scan times over a short range for: (a) 0.5%Pt/ZrO_2, (b) 0.5%Pt/$Zr_{0.9}Y_{0.1}O_{1.95}$, (c) 0.5%Pt/$Zr_{0.75}Y_{0.25}O_{1.875}$, (d) 0.5%Pt/$Zr_{0.5}Y_{0.5}O_{1.75}$, (e) 0.5%Pt/$Zr_{0.25}Y_{0.75}O_{1.625}$, (f) 0.5%Pt/$Zr_{0.1}Y_{0.9}O_{1.55}$, and (g) 0.5%Pt/$Y_2O_3$.

phase, while a higher concentration of yttrium stabilizes the cubic structure [53,54]. Shifts in the peak positions to lower 2θ values (Table 2) are consistent with macrostrain caused by Y-doping.

For the other doped catalysts, the signal is very broadened due to lower crystallinity, so it is not possible to identify the crystal structure from XRD analysis. However, analysis by XANES is helpful in elucidating the structure. XANES spectra of 0.5%Pt/Y_2O_3 and 0.5%Pt/$Zr_{0.5}Y_{0.5}O_{1.75}$ systems are shown in Fig. 2 (left and right). The zirconia spectrum for the doped system is different from that of zirconia. No shoulder is present at around 18.037 keV, and the main peak of the white line is split into two components (at 6 eV and 12 eV above the adsorption edge, respectively). These features confirm the cubic structure, and others have shown this to be the case when yttrium loadings are higher than 20% [53,54].

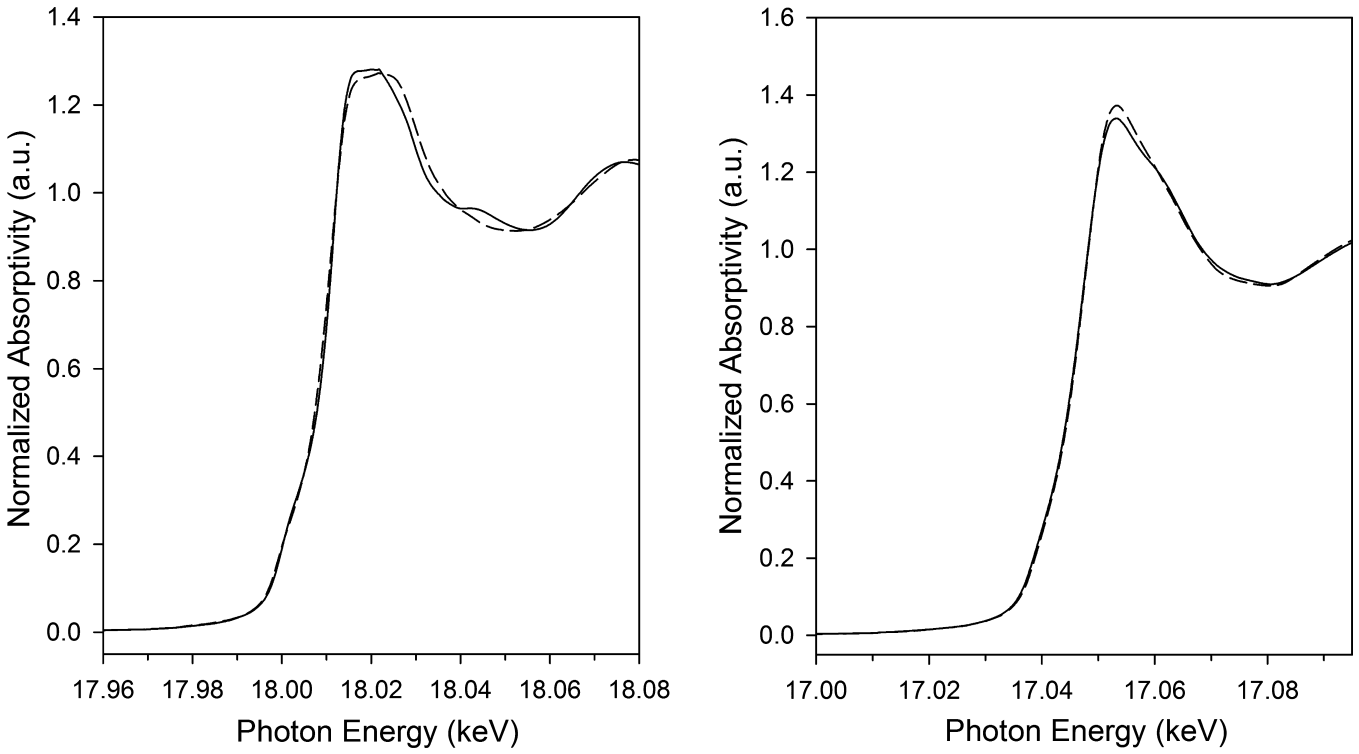

Fig. 2. Normalized XANES spectra (left) at Zr K-edge for (solid line) 0.5%Pt/ZrO_2 and (dashed line) 0.5%Pt/$Zr_{0.5}Y_{0.5}O_{1.75}$. Normalized XANES spectra at (right) Y K-edge for (solid line) 0.5%Pt/Y_2O_3 and (dashed line) 0.5%Pt/$Zr_{0.5}Y_{0.5}O_{1.75}$.

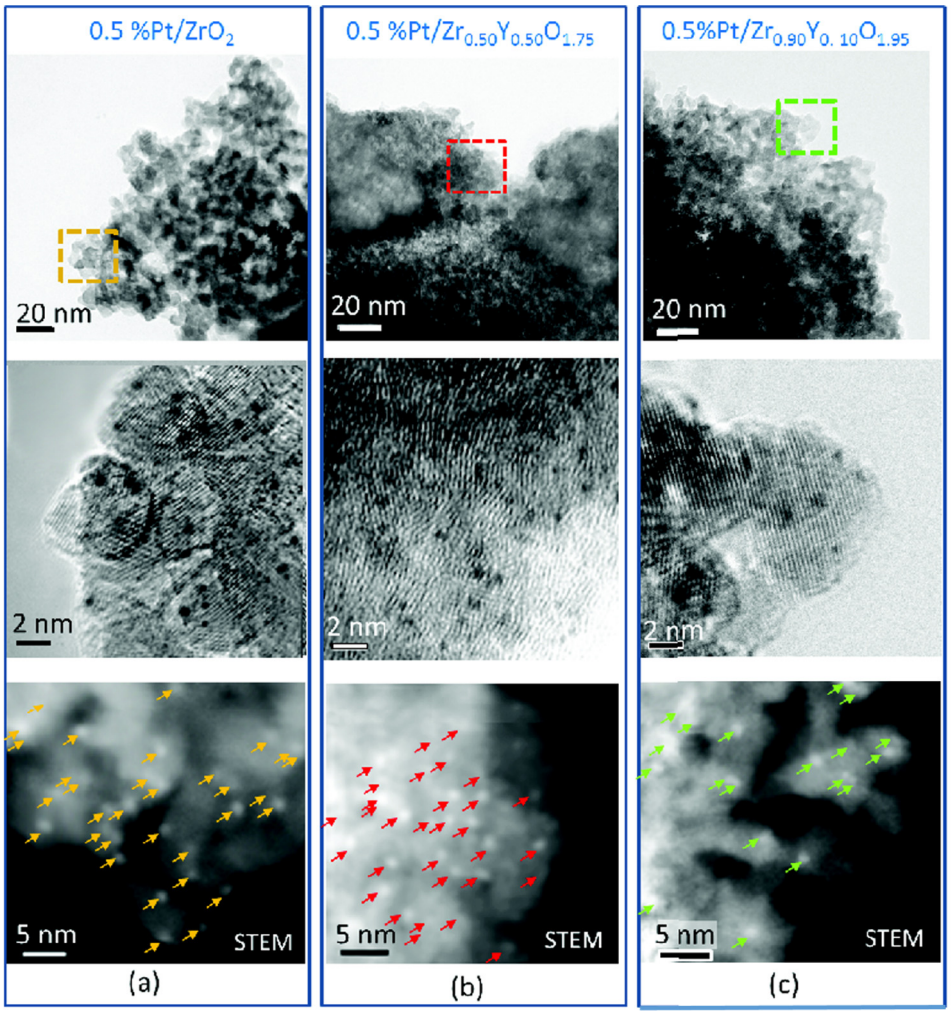

Fig. 3. (Top) TEM images reveal larger, more well-defined crystals for the (a) 0.5%Pt/ZrO_2 and (c) 0.5%Pt/$Zr_{0.90}Y_{0.10}O_{1.95}$ catalysts and a polycrystalline nature for the (b) 0.5%Pt/$Zr_{0.50}Y_{0.50}O_{1.75}$ catalyst. (middle) HR-TEM and (bottom) STEM images show that the Pt particles are well dispersed and range from 0.5 nm to 2 nm over all three supported catalysts.

The Y_2O_3 spectrum (Fig. 2, right) is characterized by two peaks of higher intensity, and the asymmetric character sug-gests a structure without significant long range ordering (e.g., nanoparticles [55]), consistent with the broad signal of the corresponding XRD profile. The spectra resemble that of the cubic structure previously reported [54]. The yttrium spectrum was also collected for the doped system (0.5%Pt/$Zr_{0.5}Y_{0.5}O_{1.75}$). The intensity for the doped system is slightly higher than Y_2O_3, and this trend has been also reported by Li et al. [54]. They observed higher intensities for the Y-doped Zr materials (3–20 mol% Y); however, the intensity continuously decreased with yttrium loading. In this work, the concentration is 50% Y and this can explain why the difference in intensities between the Y_2O_3 and the YSZ doped system is not as accentuated as in the work of Li et al. [54]. The higher intensity is typically associated with a more ionic nature of the absorbing atom, which would be consistent with a higher coordination number and longer Y—O distances [54].

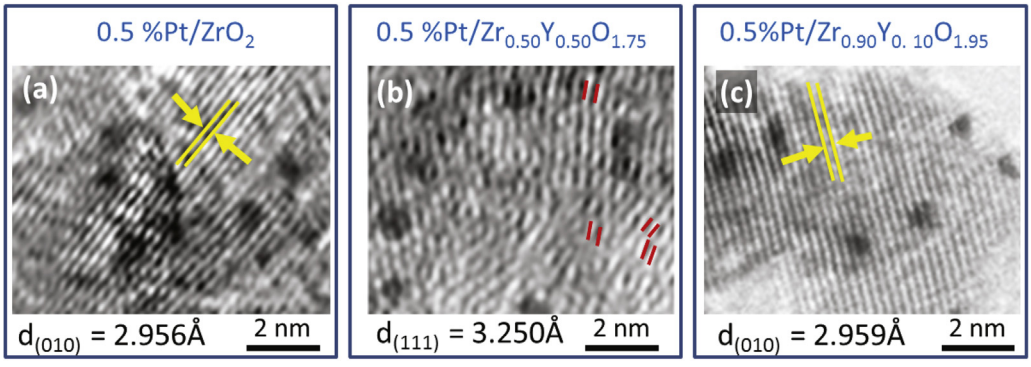

Fig. 4. High resolution TEM illustrating d-spacings. (a) and (c) show well crystallized (1 1 1) planes while (b) demonstrates a very polycrystalline nature for the cubic sample.

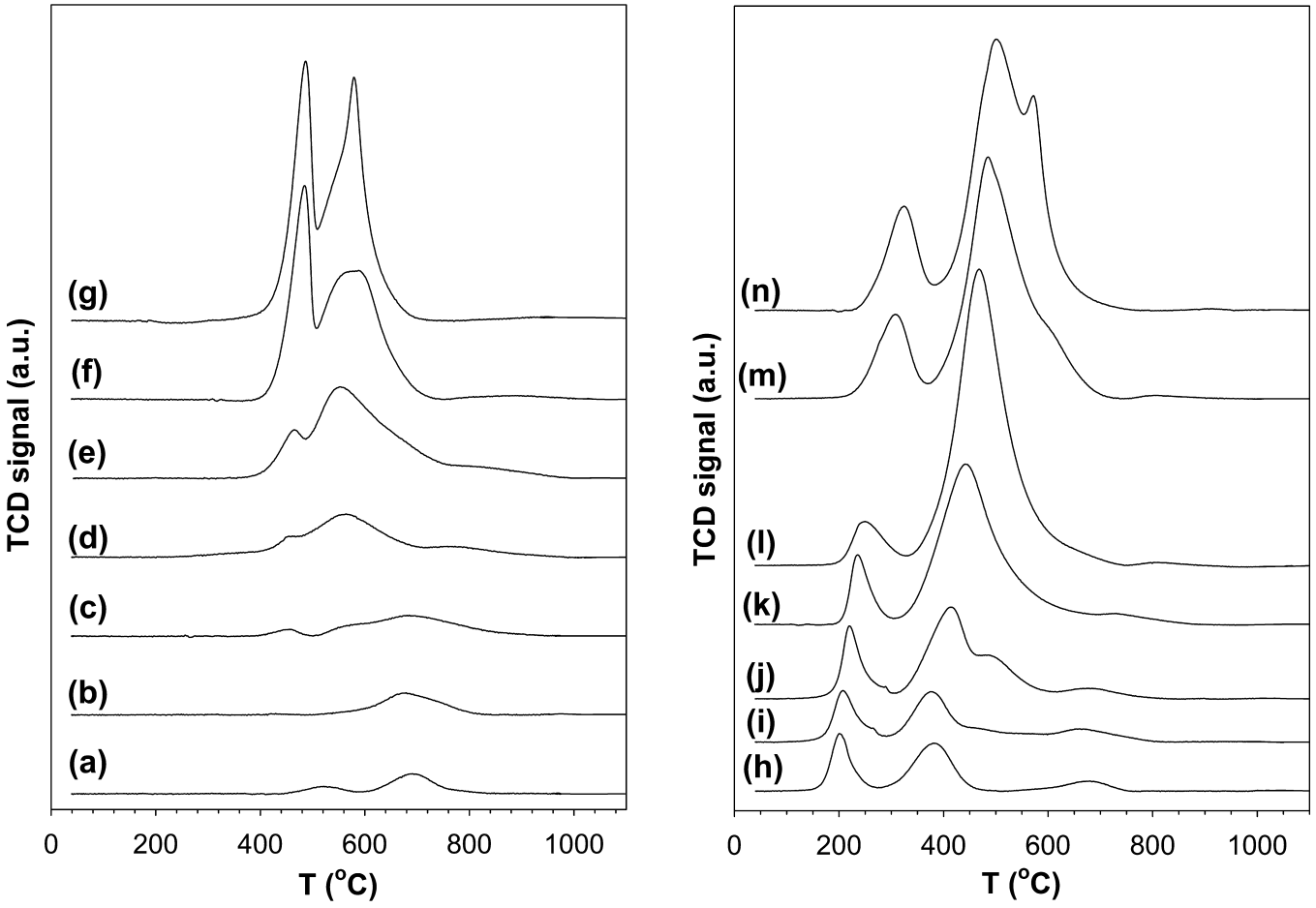

Fig. 5. Hydrogen TPR profiles for the (left) unpromoted and (right) 0.5% Pt-promoted catalysts, including: (a) ZrO_2, (b) $Zr_{0.9}Y_{0.1}O_{1.95}$, (c) $Zr_{0.75}Y_{0.25}O_{1.875}$, (d) $Zr_{0.5}Y_{0.5}O_{1.75}$, (e) $Zr_{0.25}Y_{0.75}O_{1.625}$, (f) $Zr_{0.1}Y_{0.9}O_{1.55}$, (g) Y_2O_3, (h) 0.5%Pt/ZrO_2, (i) 0.5%Pt/$Zr_{0.9}Y_{0.1}O_{1.95}$, (j) 0.5%Pt/$Zr_{0.75}Y_{0.25}O_{1.875}$, (k) 0.5%Pt/$Zr_{0.5}Y_{0.5}O_{1.75}$, (l) 0.5%Pt/$Zr_{0.25}Y_{0.75}O_{1.625}$, (m) 0.5%Pt/$Zr_{0.1}Y_{0.9}O_{1.55}$, and (n) 0.5%Pt/$Y_2O_3$.

HR-TEM images (Figs. 3 and 4) reveal larger, more well-defined crystallites for the (a) ZrO_2 and (c) $Zr_{0.90}Y_{0.10}O_{1.95}$ supports and smaller domains, with a more polycrystalline nature, for the (b) $Zr_{0.50}Y_{0.50}O_{1.75}$ support, in agreement with line broadening observed in XRD. The slight increase in the (1 1 1) d-spacing for the $Zr_{0.90}Y_{0.10}O_{1.95}$ support and lack of Y_2O_3 crystallite formation over both of the Y-doped supports suggests that a solid solution was formed in each case. This macrostrain is consistent with the shift in the XRD peaks to lower 2θ with Y doping.

In agreement with the results of EXAFS spectroscopy at the Pt L_3 edge, HR-TEM and STEM images in Fig. 3 confirm that the Pt was well dispersed. Moreover, the particle sizes, which fell within a narrow range, were similar over the three catalysts examined, with the distribution of each catalyst being 0.5–2 nm. This is critically important, as a difference in the length of the periphery of the metal-support interface has alone been identified to increase the specific rate of WGS catalysts over related Pt/ceria catalysts [3,56].

3.3. Temperature programmed reduction and TPR–XANES

The reducibility of each prepared sample was investigated by TPR experiments, and profiles are reported in Fig. 5. One complicating factor is the decomposition of surface carbonates, which is known to occur from DRIFTS studies during hydrogen reduction of ceria, zirconia, and related materials [17,22]. Another factor is that sintering most certainly occurs at the higher temperatures, which are certainly above the calcination temperature utilized in catalyst preparation. Thus, TPR is only used in a qualitative manner. The reduction of zirconia support exhibits two different peaks, respectively at ~450 °C and ~620 °C. Both of them could be ascribed to the reduction of Zr^{4+} to Zr^{3+}, which is confined to the surface of zirconia [22,57,58]. Between profiles (c) and (d), there is a distinct decrease in the temperature of the second peak. In spectrum (c), the second peak is asymmetric with a shoulder at 580 °C and a primary maximum at ~680 °C, while in spectrum (d) the primary maximum is positioned at ~570 °C with a minor tailing shoulder at 770 °C. Between profiles (e) and (g), the higher temperature shoulder of the second peak (ca. 650 °C) and tailing shoulder (770 °C) diminish and the main second peak (between 500 °C and 600 °C) increases as function of Y addition. Thus, the general trend is that the addition of Y to ZrO_2 results in a progressive shift to lower temperature. Furthermore, the incorporation of yttrium increases the uptake of H_2.

When doping ZrO_2 with yttrium, the Zr^{4+} cations in the ZrO_2 lattice are substituted by the Y^{3+} cations thereby forming oxygen vacancies to maintain charge neutrality in the lattice. The oxygen vacancies make it possible for the oxygen to move through the electrolyte by hopping from vacancy to vacancy in the lattice and one view is that this is what improves the reducibility of the sample. Surface reduction for ceria and ceria-related materials has also been found to occur by the formation of defect-associated bridging OH groups [23]. Therefore, another mechanism to consider is that the surface O atoms are converted to these Type II bridging OH groups, which is accompanied by a change in the oxidation state of the metal in the metal oxide (e.g., Zr).

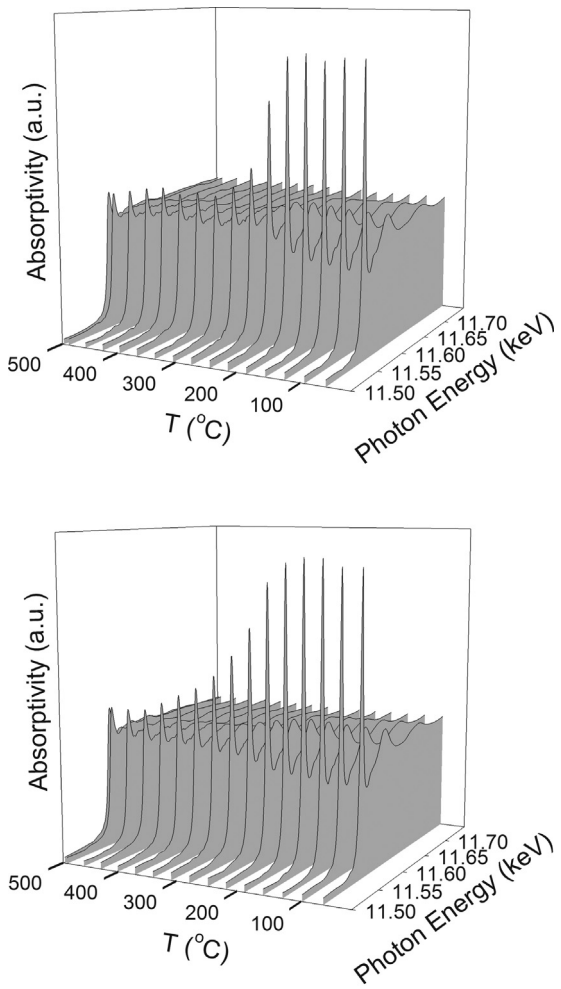

Fig. 6. TPR–XANES profiles at Pt L_{III}-edge of (top) 0.5%Pt/ZrO_2 and (bottom) 0.5%Pt/$Zr_{0.5}Y_{0.5}O_{1.75}$.

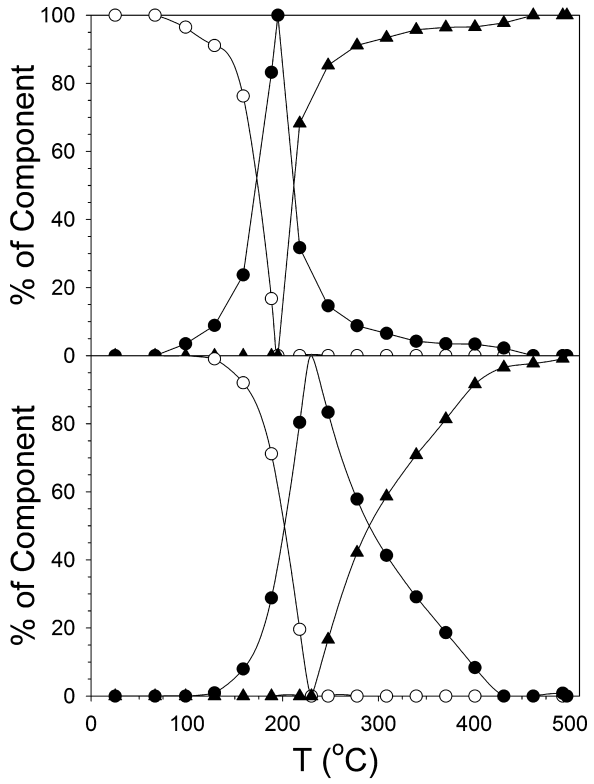

Fig. 7. (Open circles) Percentage of Pt^{4+}, (filled circles) Pt^{2+}, and (filled triangles) Pt^0 along the TPR trajectory for (top) 0.5%Pt/ZrO_2 and (bottom) 0.5%Pt/$Zr_{0.5}Y_{0.5}O_{1.75}$.

The addition of platinum on zirconia supports causes a remarkable shift in the surface reduction process to lower temperature and an increase in the uptake of hydrogen, in agreement with the work of Passos et al. [57], who carried out TPR studies on zir-conia and Pt/zirconia catalysts when screening Pt/PRO catalysts for partial oxidation of methane. Platinum may facilitate defect formation via oxygen-vacancies and subsequent dissociation of H_2O to yield bridging OH groups. Another possibility is direct dissociation of H_2 on Pt and spillover to the zirconia surface [22]. Passos et al. found that the degree of reduction of zirconia was less than 1% [57]. In order to gain further insight into the TPR peaks for the promoted catalysts, the change of oxidation state of Pt during H_2 reduction was investigated using TPR–XANES. In Fig. 6 (top) the TPR–XANES trajectories near the Pt L_{III} edge for 0.5%Pt/ZrO_2 are shown. The XANES spectra of the catalyst change significantly with increasing temperature as PtO_2 converted to PtO and then to Pt^0. Platinum reduction occurs between 140 °C and 300 °C and then is virtually completely reduced to metal. The TPR–XANES trajectory of 0.5%Pt/ZrO_2 indicates that at least part of the first peak in Fig. 5 (plot h), which occurs between the 142 °C and 270 °C, corresponds to the reduction of Pt oxide, while the other two peaks at higher temperature are likely associated with reduction of Zr^{4+} to Zr^{3+} on the surface, which also involves surface carbonate decomposition [22]. In agreement with the work of Passos et al. [57] and Jozwiak [58], metal promoter addition shifts the two peaks to lower temperatures than those of unpromoted zirconia, and the increase in intensity indicates that the extent of reduction of zirconia is also increased.

Passos et al. [57] observed that the extent of reduction of Pt/yttria was ~4%, which is significantly higher than that of Pt/zirconia and correlates well with the increase in intensity observed in Fig. 5 with increases in yttria doping. Thus, by increas-ing the yttrium loading the platinum appears to increase more the extent of reduction of the supports, especially for the systems where the fraction of yttrium is between 0.1 and 0.75, although the shifts of the peaks to lower temperature become less pronounced with yttria addition. This is in good agreement with the TPR results of Passos et al. [57], where peak shifts were less significant for Pt/yttria relative to Pt/zirconia. The H_2-TPR–XANES for the sys-tem 0.5%Pt/$Zr_{0.5}Y_{0.5}O_{1.75}$ is shown at the bottom of Fig. 6. In this case, Pt reduction was only completed by 400 °C. One complicat-ing factor is the metal-support interaction. Since the mixed oxide had a higher surface area, more Pt may be required to overcome the metal-support interaction. As in the case of 0.5%Pt/ZrO_2, the results from TPR–XANES indicate that a fraction of the first peak in Fig. 5 (plot k) is associated with reduction of platinum oxide.

Linear combination fittings were performed using PtO_2, PtO (generated from the point of 50% reduction of PtO_2), and Pt^0 reference spectra and the fitting results are shown in Fig. 7. Reduction of both PtO_2 to PtO and PtO to Pt^0 were at higher temperatures for the 0.5%Pt/$Zr_{0.5}Y_{0.5}O_{1.75}$ catalyst relative to the Pt/ZrO_2 catalyst.

To investigate the local atomic structure of Pt, EXAFS was also performed. The results of the modeling procedure using FEFFIT for the k-weighted EXAFS Fourier transform and filtered k-weighted χ (k) spectra of Pt-promoted catalyst following TPR experiment and cooling to ambient conditions are shown in Fig. 8. The fitting parameters are summarized in Table 3. The presence of Pt–$O_{support}$ coordination and low Pt–Pt metal coordination numbers indicate that the Pt particles were highly dispersed on both catalysts.

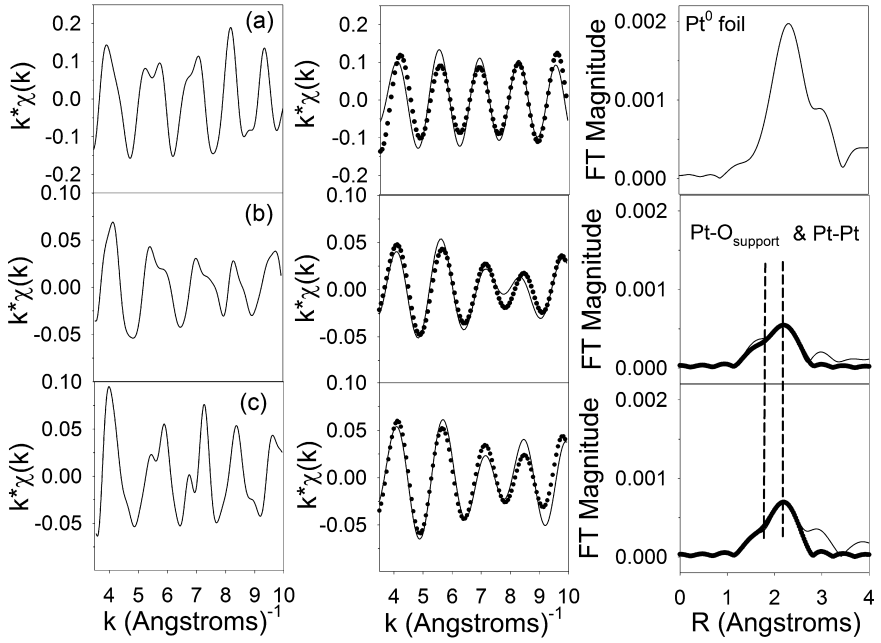

Fig. 8. (Solid lines) EXAFS spectra following the TPR experiment after catalysts were cooled to close to ambient temperature and (filled circles) resulting fitting for (a) Pt metal foil (b) 0.5%Pt/ZrO_2 and (c) 0.5%Pt/$Zr_{0.5}Y_{0.5}O_{1.75}$, including (left) unfiltered $k^*\chi$(k); (middle) (solid line) filtered $k^*\chi$(k) spectra and (filled circles) resulting fitting; and (right) (thin line) k-weighted Fourier Transform magnitude spectra and (filled circles) resulting fitting.

3.4. EXAFS and XANES under H_2 reduction conditions

The Fourier Transform magnitude spectra of zirconia have two peaks. The first peak corresponds to the contribution of the first oxygen shell around the Zr absorber, while the second peak contains information related to Zr–Zr coordination. At the same temperature, different parameters can influence the intensity of these peaks such as: the degree of reduction, the crystallite size [59], and the local order in the system [60].

Chadwick et al. [60] concluded it is not possible to identify the exact nature of the disorder. Origins of disorder could be: (i) the presence of a large number of defects and surface atoms; (ii) highly disordered interfaces between crystallites; and (iii) the existence of an amorphous phase. The higher degree of disorder in the doped system is likely due to a higher number of defects associated with the presence of yttrium. The addition of a trivalent oxide such as Y_2O_3 to ZrO_2 induces the formation of lattice defects, including oxygen vacancies V_o^{2+} and negatively charged substitutional solutes Y_{Zr^-}, in the zirconia lattice [61]. The vacancies are formed to maintain charge neutrality in the lattice because the Zr^{4+} cations in the ZrO_2 lattice are substituted by the Y^{3+} cations.

Results of the modeling procedure using FEFFIT for the k-weighted EXAFS Fourier transform and filtered k-weighted χ (k) spectra of the Pt-promoted catalyst at 400 °C are reported in Fig. 9 for Zr and Y K-edge data. The condition selected should be close to that of the water-gas-shift testing condition (reduction for 1 h at 350 °C), considering that a relatively faster ramp was used, as well as a lower concentration of H_2. The solid lines show the experimental data, while the filled circles indicate the best fit. The fitting parameters are summarized in Table 4 and include both catalysts and supports. The fitting ranges were approximately Δk = 3.5–10.0Å^{-1} (Zr) and 3.9–10Å^{-1} (Y) and ΔR = 1.0–4.0Å. S_0^2 = 0.9. Since e_0 is highly correlated with N, values were previously selected to give nominal distances corresponding to each crystal structure. Distances were constrained to float in the vicinity of nominal values. Coordination numbers were fixed to their nominal values and complete mixing of Zr and Y was assumed in the mixed oxide. Results show that good fits could be obtained for each crystal structure identified, with the r-factor always being lower than 0.02. The value obtained for the Deybe–Waller factor is higher for the doped system consistent with a more disordered structure. Thus, the results provide further confirmation that while the Pt/ZrO_2 catalyst exhibited the tetragonal structure, doping the zirconia with yttria results in a change to the cubic structure at the 50% Y-doping level.

The Zr and Y K-edge XANES spectra and their derivatives for Pt promoted catalysts treated at 400 °C in H_2 are reported in Fig. 10. The spectra of reference compounds for Zr^{4+} (ZrO_2), Zr^{3+} (ZrN) and the metal (Zr^0) have also been included for purpose of comparison. For Zr K-edge data, a comparison between 0.5%Pt/ZrO_2 and 0.5%Pt/$Zr_{0.5}Y_{0.5}O_{1.75}$ shows that the doped system, which has a cubic structure, has a more pronounced change during reduction and is likely due in part to the formation of defects (e.g., vacancies and associated bridging OH groups), which are present at or

Table 3
Results of EXAFS fitting parameters for reduced catalysts acquired near the Pt L_{III}-edge. The fitting ranges were approximately Δk = 3.0–10.0 Å^{-1} and ΔR = 1.4–2.75 Å. S_0^2 = 0.9.

Sample description	N Pt—$O_{Support}$	R Pt—$O_{Support}$ (Å)	N Pt—Pt	R Pt—Pt (Å)	e_0 (eV)	σ^2 (Å^2)	r-Factor
Pt^0 foil	–	–	**12**	2.763 (0.0132)	4.35 (20.1)	0.00696 (0.000927)	0.02
0.5%Pt/ZrO_2	0.56 (0.26)	1.922 (0.149)	3.24 (0.663)	2.708 (0.0140)	10.3 (1.20)		
0.5%Pt/$Y_{0.50}Zr_{0.50}O_{1.75}$	0.52 (0.28)		4.22 (0.763)				

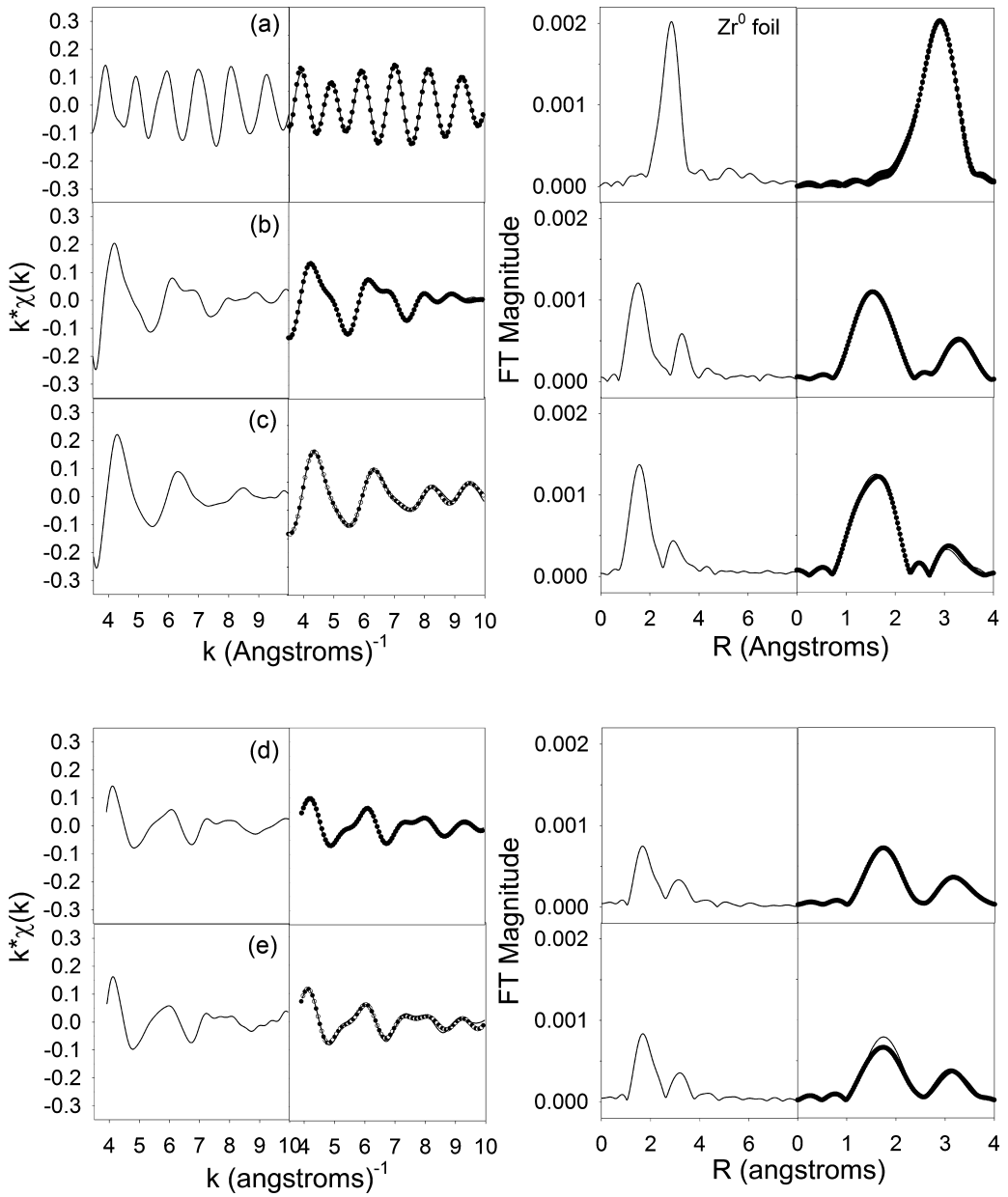

Fig. 9. (solid lines) EXAFS spectra at 400 °C at the Zr K-edge for (a) Zr metal foil; (b) 0.5%Pt/ZrO_2; and (c) 0.5%Pt/$Zr_{0.5}Y_{0.5}O_{1.75}$, and at the Y K-edge for (d) 0.5%Pt/Y_2O_3; and (e) 0.5%Pt/$Zr_{0.5}Y_{0.5}O_{1.75}$, including (left) unfiltered $k^*\chi$(k); (middle) (solid line) filtered $k^*\chi$(k) spectra and (filled circles) resulting fitting; and (right) (thin line) k-weighted Fourier Transform magnitude spectra and (filled circles) resulting fitting.

near the surface of the oxide. XANES intensities of yttria were also observed to decrease with temperature (Fig. 10). Changes may not be due solely to partial reduction, but may also include enhanced crystalline ordering with temperature, as has been observed previously with yttria [56].

3.5. Catalytic testing using a fixed bed reactor

Fig. 11 shows the WGS activity versus reaction temperature. The results show that the oxide support has a strong influence on the WGS activity. One possibility is that the greater number of defects in the Y-doped systems increases the population of defect-associated bridging OH groups or O-vacancy sites, resulting in a greater number of sites for associative or redox mechanisms. Another possibility is that the strain in the zirconia lattice by Y doping improves the O-mobility, and in turn, the mobility of the O-bound intermediate which migrates to and decompose at the Pt-oxide interface; or, in the case of a redox mechanism, the O adatom may be released more easily by reaction with CO. All of the prepared catalysts were active for the WGS reaction. The yttrium supported Pt catalyst resulted in the worst performance. However, the addition of yttrium improved the performance of zirconia when the loading was at or lower than 50%. Higher loadings decreased the conversion, and may be due to changes in the reducibility of the sample (i.e., toward higher temperature). Moreover, higher yttrium concentrations could create oxygen vacancies bonded to two cations, thus decreasing the mobility of oxygen. At 300 °C, CO conversion for 0.5%Pt/ZrO_2 was 44.8% and it increased from 50% to 74% by decreasing the yttrium loading from 50% to 10%.

3.6. Diffuse reflectance Fourier transform infrared spectroscopy

One proposed mechanism for water-gas-shift is that the catalyst operates by transport and decomposition of associated O-bound

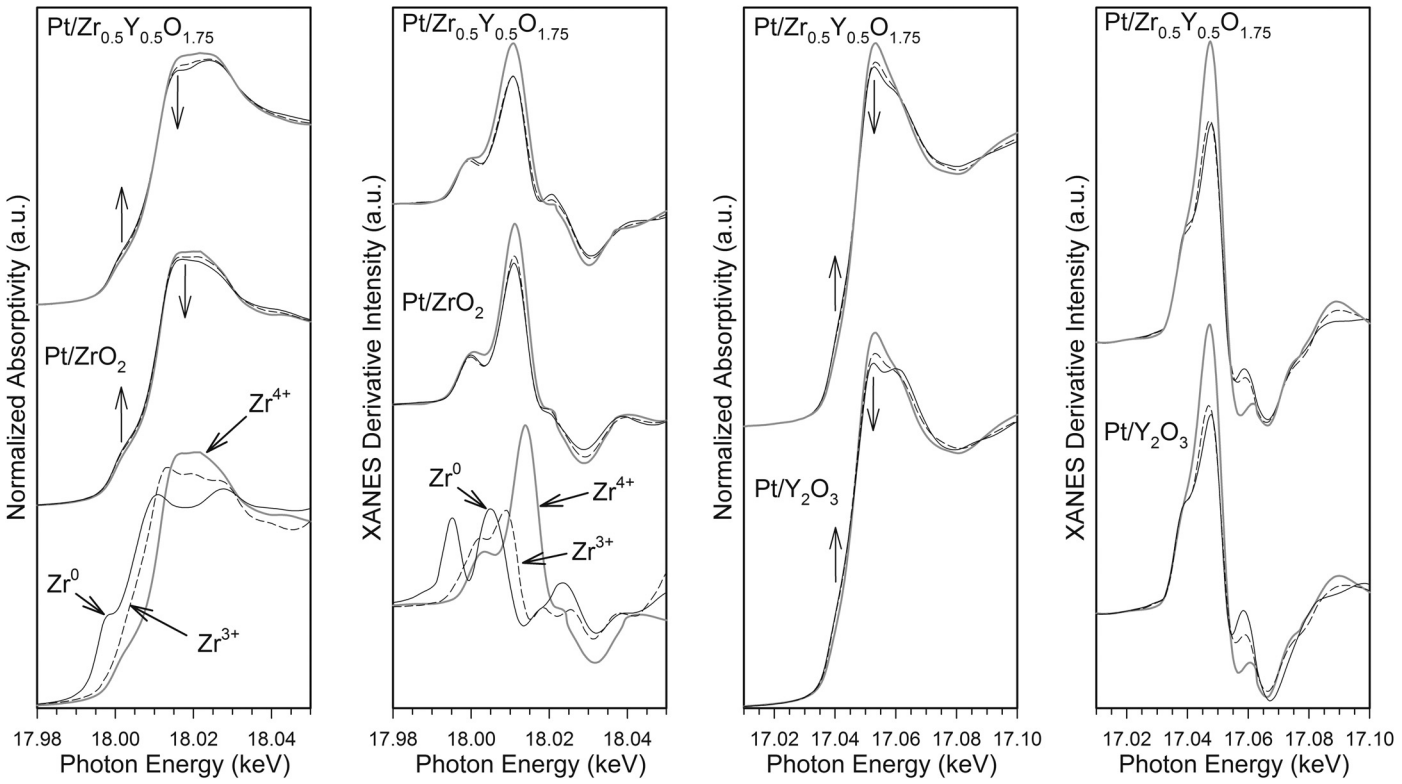

Fig. 10. (a, b) Zr K-edge and (c, d) Y K-edge XANES (a, c) normalized and (b, d) derivative spectra for (a, b) Pt/ZrO_2 and $Pt/Zr_{0.5}Y_{0.5}O_{1.75}$ and (c, d) Pt/Y_2O_3 and $Pt/Zr_{0.5}Y_{0.5}O_{1.75}$ at (thick gray) room T; (dashed) H_2, 400 °C and (solid line) H_2, 840 °C. References: Zr^0, ZrN (Zr^{3+}), and ZrO_2.

species (e.g., formates, carbonates, and/or carboxylates) from the oxide component, where they are formed to the metal-oxide particle, where the metal is involved in the dehydrogenation and catalyzes their decomposition. One of the first proposals of such a mechanism was that of Grenoble et al. [62]. With related Pt/ceria catalysts, Jacobs et al. [17] showed that under steady state conditions whereby the H_2O/CO ratio was high to favor first order

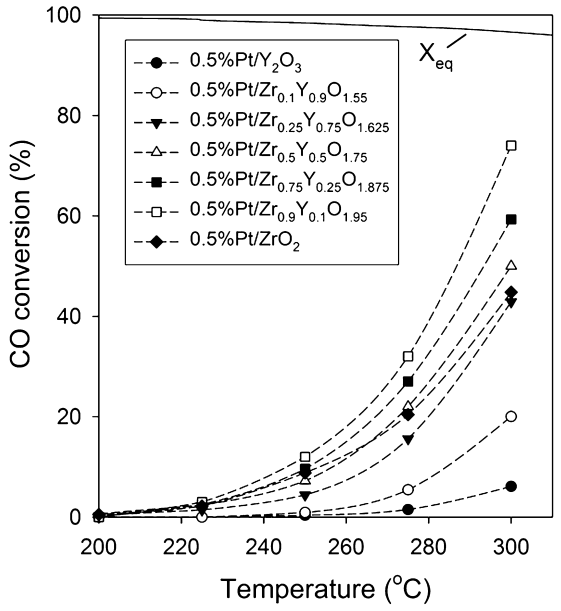

Fig. 11. Carbon monoxide conversion as a function of temperature for different yttrium loadings, including (a) $0.5\%Pt/Y_2O_3$; (b) $0.5\%Pt/Zr_{0.1}Y_{0.9}O_{1.55}$; (c) $0.5\%Pt/Zr_{0.25}Y_{0.75}O_{1.625}$; (d) $0.5\%Pt/Zr_{0.5}Y_{0.5}O_{1.75}$; (e) $0.5\%Pt/Zr_{0.75}Y_{0.25}O_{1.875}$; (f) $0.5\%Pt/Zr_{0.9}Y_{0.1}O_{1.95}$; and (g) $0.5\%Pt/ZrO_2$.

kinetic behavior by CO and zero order behavior by H_2O, the formate steady state coverage was more rate-limited with increasing Pt content and suggested a role by Pt in facilitating formate dehydrogenation during its forward decomposition (i.e., reactant-promoted by steam as proposed by Shido and Iwsawa [7]) in H_2O. Meunier et al. [63] have suggested that formate species observed by infrared spectroscopy are not kinetically relevant, as in some cases, the total formate band exchanged, albeit at a slower rate than the CO_2 signal in ^{12}CO to ^{13}CO switching tests during WGS. As for-mate species decompose rapidly in steam at temperatures as low as 130–140 °C in transient formate decomposition tests [8,27,28], we have argued against part of the logic, as the total formate band under steady state low temperature WGS conditions should contain both the signal of both rapidly reacting formates in the vicinity of Pt (having low rate-limited coverage), as well as the signal of slowly reacting formates on the support which may be classified as kinetically irrelevant spectator species during steady state iso-tope switching [64]. Moreover, a rapid Pt-carbonyl switch in the isotope tracer measurements should not immediately be taken as evidence of a redox mechanism involving the reaction of Pt-CO with the support O adatoms; replacing H_2O in the WGS feed with inert gas also leads to a rapid switching rate for Pt carbonyl, but this is merely a replacement process, and there is no reason why such a replacement process should not occur during WGS as well [10]. The group of Efstathiou [65–68] has indicated, using iso-topic tracers, that the pool of carbon-containing intermediates may reside within a zone of 5–10 Å (1–2 lattice constants of the support) around each Pt nanoparticle. The reason is that the C-pool was found to be considerably larger than one monolayer of Pt. If that is the case, and if there are less reactive species (e.g., formate) present on the support further from Pt that must diffuse prior to turnover at the metal-support interface, then one should expect the total formate signal (i.e., slowly reacting and rapidly reacting) to lag that of CO_2 in infrared spectroscopy investigations

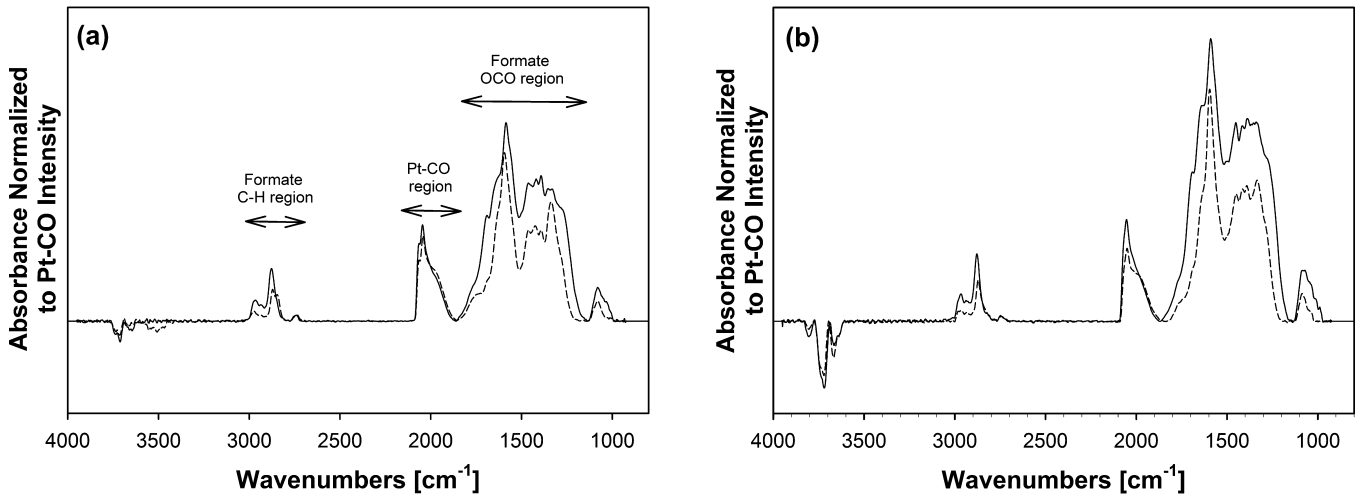

Fig. 12. Steady state formate and Pt—CO band intensities during the CO adsorption (solid line) and after the formate decomposition (dotted line) for (a) 0.5%Pt/ZrO_2 and 0.5%Pt/$Zr_{0.9}Y_{0.1}O_{1.95}$.

involving ^{12}CO to ^{13}CO switching. However, this by no means rules out formate, formed on the support adjacent to Pt and decomposed at the metal-support junction, as an important intermediate. That is, the same chemical species (in this case, formate) may be a spectator when formed at one location of the catalyst (e.g., the support) but serve as an intermediate when formed at a different location (e.g., the metal-support junction).

The impact of yttrium doping on one representative O-bound species, formate, was carried out at a temperature of 130 °C utilizing a very low water concentration. Fig. 12 shows spectra following CO adsorption/He purging, where formates are generated from the reaction of CO with defect-associated bridging OH groups for the 0.5%Pt/ZrO_2 and 0.5%Pt/$Zr_{0.9}Y_{0.1}O_{1.95}$ catalysts. The main bands for formates are the ν(CH) band (2880 cm^{-1}) and the ν(OCO) asymmetric (1585 cm^{-1}) and symmetric (1390 cm^{-1}) stretching bands [22,27,28]. The Pt carbonyl bands extend from 1900 to 2100 cm^{-1} and displayed similar asymmetric character for both catalysts. Both EXAFS measurements at the L_3 edge and STEM imaging revealed that the Pt crystallite size was, on average, similar between the two catalyst samples. The ratio of the formate/Pt-CO bands for 0.5%Pt/$Zr_{0.9}Y_{0.1}O_{1.95}$/0.5%Pt/ZrO_2 = 1.25, suggesting a significant increase in the number of defect-associated bridging OH groups for the Y-doped catalyst. The greater decrease of the band associated with ν(OH) intensity upon CO adsorption is also consistent with the greater formate band intensity associated with the Y-doped catalyst. Fig. 13 also shows the formate bands during the purge in helium after forward-formate decomposition in steam (with CO_2 evolution) at 130 °C for the sample 0.5%Pt/ZrO_2 and the sample with the best catalytic activity, 0.5%Pt/$Zr_{0.9}Y_{0.1}O_{1.95}$. The ratio of the formate band areas before and after steaming for the 0.5%Pt/ZrO_2 and 0.5%Pt/$Zr_{0.9}Y_{0.1}O_{1.95}$ catalysts are 0.67 and 0.56, respectively, suggesting that the formate decomposition is more rapid on the Y-doped catalyst. The faster rate of change of the ν(CH) band intensity during formate decomposition (Fig. 13) provides further evidence. No significant difference was observed in Pt dispersion; however, a higher defect concentration leads to a higher coverage of formate on the catalyst during CO adsorption. Thus, a higher formate coverage (albeit rate-limited) during WGS would alone influence the rate. Another possible factor is that a more rapid formate decomposition rate may be consistent with higher surface O-mobility for the Y-doped catalyst, since formates are bound to the surface of the oxide by their O atoms. The transient formate decomposition results in steam show that formate reaches a stagnant coverage faster with the undoped catalyst, while

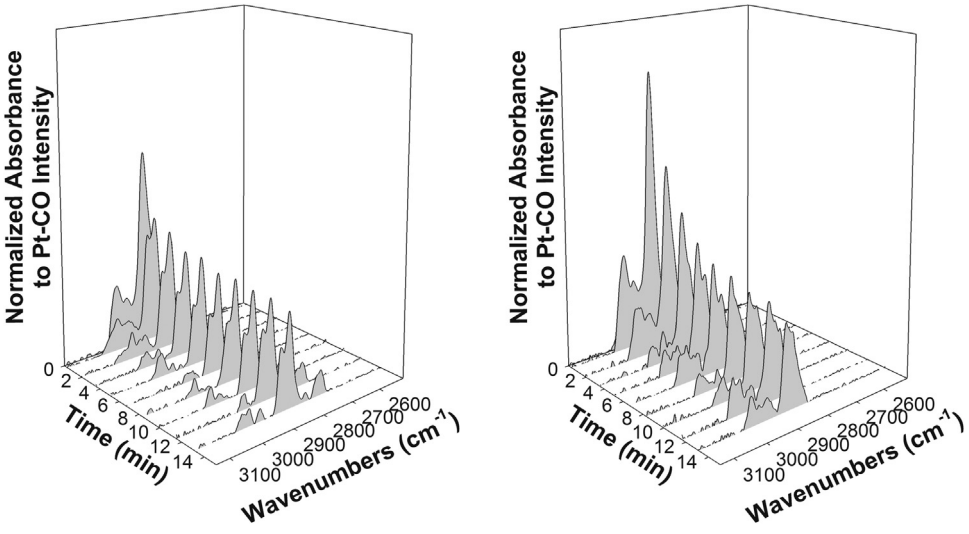

Fig. 13. Transient forward formate decomposition in a low concentration of steam for (left) 0.5%Pt/ZrO_2 and (right) 0.5%Pt/$Zr_{0.9}Y_{0.1}O_{1.95}$.

Table 4
Results of EXAFS fitting parameters for reduced catalysts acquired near the Zr and Y K-edges during H_2 treatment at 400 °C.

Sample description	*N* Zr—O	*R* Zr—O (Å)	σ^2 (Å^2)	*N* Zr—Zr	*R* Zr—Zr (Å)	σ^2 (Å^2)	*NZr—Y*	*RZr—Y* (Å)	σ^2 (Å^2)	*NY—O*	*RY—O* (Å)	σ^2 (Å^2)	*N* Y—Y	*R* Y—Y (Å)	σ^2 (Å^2)	*r*-Factor
Zr^0 foil (ambient)	-	-	-	6.0	3.16	0.005	–	–	–	–	–	–	–	–	–	0.001
				6.0	3.26	0.006										
ZrO_2	4.0	2.13	0.004	4.0	3.59	0.017	–	–	–	–	–	–	–	–	–	0.004
	4.0	2.31	0.009	8.0	3.63	0.017										
0.5%Pt/ZrO_2	4.0	2.13	0.003	4.0	3.59	0.018	–	–	–	–	–	–	–	–	–	0.004
	4.0	2.31	0.008	8.0	3.63	0.018										
Y_2O_3	–	–	–	–	–	–	–	–	–	6.0	2.27	0.008	6.0	3.49	0.019	0.019
													6.0	3.93	0.019	
0.5%Pt/Y_2O_3	–	–	–	–	–	–	–	–	–	6.0	2.27	0.008	6.0	3.46	0.019	0.015
													6.0	3.93	0.019	
$Y_{0.50}Zr_{0.50}O_{1.75}$	7.0	2.16	0.013	6.0	3.48	0.025	6.0	3.51	0.025	7.0	2.26	0.015	6.0	3.55	0.019	0.02
0.5%Pt/$Y_{0.50}Zr_{0.50}O_{1.75}$	7.0	2.14	0.012	6.0	3.44	0.023	6.0	3.48	0.024	7.0	2.29	0.017	6.0	3.51	0.020	0.02

The fitting ranges were approximately $\Delta k = 3.5–10.0$ Å^{-1} (Zr) and 3.9–10 Å^{-1} (Y) and $\Delta R = 1.0–4.0$ Å. $S_0^2 = 0.9$. Since e_0 is highly correlated with *N*, values were selected to give nominal distances corresponding to each crystal structure identified by XRD and XANES. Distances were constrained to float in the vicinity of nominal values. Coordination numbers were fixed to their nominal values and complete mixing of Zr and Y was assumed in the mixed oxide. Results show that good to excellent fits could be obtained for each crystal structure identified.

with the Y-doped catalyst, the formate continues to diffuse and react over a longer time interval. The result may suggest a slight extension of the reactive zone around Pt metal particles; however, additional research is required to demonstrate that aspect conclusively. Thus, as has been found to be the case with Pt/ceria catalysts, where Ca [36] and La [67] doping (at the 20% level) has found to further improve catalytic activity, the present case underscores the fact that Pt/zirconia, which is of great interest as a fuel processor catalyst, can similarly be improved by doping, in this case with Y (especially at the 10% level).

4. Conclusions

Nano-scale Y-doped zirconium oxide materials were prepared with high surface areas (150–200 m^2/g) and small nanocrystallites. A combination of XANES and EXAFS was used to show that ZrO_2 exhibited the tetragonal phase, while the $Zr_{0.5}Y_{0.5}O_{1.75}$ support displayed the cubic phase. A comparison of diffraction profiles between undoped zirconia and $Zr_{0.9}Y_{0.1}O_{1.95}$ suggests that the $Zr_{0.9}Y_{0.1}O_{1.95}$ support was tetragonal in structure. A slight increase in d-spacing observed in HR-TEM for the $Zr_{0.9}Y_{0.1}O_{1.95}$ support relative to undoped ZrO_2, along with a shift to lower 2θ in XRD, provide evidence that Y-doping caused macrostrain.

EXAFS results at the Pt L_3 edge (0.5%Pt/ZrO_2 and 0.5%Pt/$Y_{0.5}Zr_{0.5}O_{1.75}$) and STEM imaging of 0.5%Pt/ZrO_2, 0.5%Pt/$Zr_{0.9}Y_{0.1}O_{1.95}$, and 0.5%Pt/$Y_{0.5}Zr_{0.5}O_{1.75}$ catalysts, demonstrate that the Pt clusters were highly dispersed and similar in size. STEM images revealed no difference in the ranges of Pt diameters; that is, each catalyst exhibited a narrow size distribution of 0.5–2 nm.

With increasing Y-doping levels, the peaks of surface reduction shifted to lower temperature. Pt addition facilitated surface reduction further, but more so for the catalysts with higher Zr content. Consistent with H_2-TPR profiles, TPR–XANES results at the Pt L_{III}-edge showed that the platinum oxides reduced at a slightly lower temperature on the 0.5%Pt/ZrO_2 catalyst relative to the 0.5%Pt/$Y_{0.5}Zr_{0.5}O_{1.75}$ catalyst, and this may be due to the greater surface area and smaller average support domain size associated with the doped catalyst (e.g., an increased metal-support interaction).

The higher concentration of surface defects for the 0.5%Pt/$Zr_{0.9}Y_{0.1}O_{1.95}$ catalyst relative to 0.5%Pt/ZrO_2 was confirmed by DRIFTS of adsorbed CO, while a greater surface mobility of surface formate was suggested based on forward formate decomposition experiments in steam. The Y-doped Pt promoted catalysts displayed higher water-gas-shift activities relative to the 0.5%Pt/ZrO_2 catalyst when the Y content was at or below 50%. The system with the best catalytic performance was 0.5%Pt/$Zr_{0.9}Y_{0.1}O_{1.95}$. The results suggest that new alkali-doped Pt/zirconia catalysts might be further improved by doping zirconia with yttria, and this will be explored in the near future.

Acknowledgments

Experiments conducted at UK-CAER were supported by the Commonwealth of Kentucky. We further acknowledge the financial support of the Italian Ministry of Education, Universities and Research for the scholarship of Dr. Michela Martinelli. This research was carried out, in part, at the National Synchrotron Light Source, Brookhaven National Laboratory, which is supported by the US DOE, Division of Materials Science and Chemical Science. Argonne's research was supported in part by the U.S. DOE, Office of Fossil Energy, NETL. The use of the APS was supported by the U.S. DOE, Office of Science, Office of Basic Energy Sciences, under Contract No. DE-AC02-06CH11357. MRCAT operations are supported by the DOE and the MRCAT member institutions.

References

[1] A.F. Ghenciu, Curr. Opin. Solid State Mater. Sci. 6 (2002) 389–399.
[2] R. Farrauto, S. Hwang, L. Shore, W. Ruettinger, J. Lamper, T. Giroux, Annu. Rev. Mater. Res. 33 (2003) 1–27.
[3] G. Jacobs, B.H. Davis, in: J.J. Spivey (Ed.), Catalysis, vol. 20, RSC Publishing, London, UK, 2007, pp. 122–285.
[4] S. Hilaire, X. Wang, T. Luo, R.J. Gorte, J. Wagner, Appl. Catal. A: Gen. 215 (2001) 271–278.
[5] Y. Li, Q. Fu, M. Flytzani-Stephanopoulos, Appl. Catal. B: Environ. 27 (2000) 179–191.
[6] C.M. Kalamaras, D.D. Dionysiou, A.M. Efstathiou, ACS Catal. 2 (2012) 2729–2742.
[7] T. Shido, Y. Iwasawa, J. Catal. 141 (1993) 71–81.
[8] G. Jacobs, P.M. Patterson, U.M. Graham, D.E. Sparks, B.H. Davis, Appl. Catal. A: Gen. 269 (2004) 63–73.
[9] G. Jacobs, S. Khalid, P.M. Patterson, D.E. Sparks, B.H. Davis, Appl. Catal. A: Gen. 268 (2004) 255–266.
[10] G. Jacobs, A.C. Crawford, B.H. Davis, Catal. Lett. 100 (2005) 147–152.
[11] J.M. Pigos, C.J. Brooks, G. Jacobs, B.H. Davis, Advances in Fischer–Tropsch Synthesis, Catalysts and Catalysis, CRC, Press, Taylor & Francis Group, Boca Raton, FL, 2010, pp. 365–394 (Chapter 19).
[12] J. Vecchietti, A. Bonivardi, W. Xu, D. Stacchiola, J.J. Delgado, M. Calatayud, S.E. Collins, ACS Catal. 4 (2014) 2088–2096.
[13] F.C. Meunier, D. Tibiletti, J.P. Breen, R.J. Burch, J. Phys. Chem. B 108 (2004) 20240–20246.
[14] Y. Chen, H. Wang, R. Burch, C. Hardacre, P. Hu, Faraday Discuss. 152 (2011) 121–133.
[15] X.Q. Gong, P. Hu, R. Raval, J. Chem. Phys. 119 (2003) 6324–6334.
[16] K. Mudiyanselage, S.D. Senanayake, L. Feria, S. Kundu, A.E. Baber, J. Graciani, A.B. Vidal, S. Agnoli, J. Evans, R. Chang, S. Axnanda, Z. Liu, J.F. Sanz, P. Liu, J.A. Rodriguez, D. Stacciola, J. Angew. Chem. 52 (2013) 5101–5105.
[17] G. Jacobs, U.M. Graham, E. Chenu, P.M. Patterson, A. Dozier, B.H. Davis, J. Catal. 229 (2005) 499–512.
[18] A. Goguet, F. Meunier, J.P. Breen, R. Burch, M.I. Petch, A.F. Ghenciu, J. Catal. 226 (2004) 382–392.
[19] X. Liu, W. Ruettinger, R. Farrauto, Appl. Catal. B: Environ. 56 (2005) 69–75.
[20] K.Y. Hwang, S.K. Ihm, S.C. Park, J.S. Park, Int. J. Hydrogen Energy 38 (2013) 6044–6051.
[21] K.G. Azzam, I.V. Babich, K. Seshan, L. Lefferts, J. Catal. 251 (2007) 163–171.
[22] E. Chenu, G. Jacobs, A.C. Crawford, R.A. Keogh, P.M. Patterson, D.E. Sparks, B.H. Davis, Appl. Catal. B: Environ. 59 (2005) 45–56.
[23] C. Binet, M. Daturi, J.-C. Lavalley, Catal. Today 50 (1999) 207–225.
[24] H. Iida, A. Igarashi, Appl. Catal. A: Gen. 303 (2006) 192–198.
[25] H. Iida, A. Igarashi, Appl. Catal. A: Gen. 298 (2006) 152–160.
[26] C.J. Brooks, A. Hagemeyer, K. Yaccato, R. Carhart, M. Herrmann, 19th North Am. Catal. Soc. Meeting, May 22–27, Philadelphia, PA, USA, 2005.
[27] J.M. Pigos, C.J. Brooks, G. Jacobs, B.H. Davis, Appl. Catal. A: Gen. 319 (2007) 47–57.
[28] J.M. Pigos, C.J. Brooks, G. Jacobs, B.H. Davis, Appl. Catal. A: Gen. 328 (2007) 14–26.
[29] D. Nguyen-Thanh, A.M. Duarte de Farias, M.A. Fraga, Catal. Today 138 (2008) 235–238.
[30] J. Goscianska, M. Ziolek, E. Gibson, M. Daturi, Appl. Catal. B: Environ. 97 (2010) 49–56.
[31] G. Balducci, M. Saiful Islam, J. Kaspar, M. Fornasiero, M. Graziani, Chem. Mater. 15 (2003) 3783–3787.
[32] G. Balducci, J. Kaspar, M. Fornasiero, M. Graziani, M. Saiful Islam, J.D. Gale, J. Phys. Chem. B 101 (1997) 1750–1753.
[33] G. Balducci, J. Kaspar, M. Fornasiero, M. Graziani, J. Phys. Chem. B 102 (1998) 557–561.
[34] G. Balducci, M. Saiful Islam, J. Kaspar, M. Fornasiero, M. Graziani, Chem. Mater. 12 (2000) 677–681.
[35] B.C.H. Steele, Solid State Ionics 129 (2000) 95–110.
[36] L.Z. Linganiso, G. Jacobs, K.G. Azzam, U.M. Graham, B.H. Davis, D.C. Cronauer, A.J. Kropf, C.L. Marshall, Appl. Catal. A: Gen. 394 (2011) 105–116.
[37] W.P. Dow, Y.P. Piao, T.J. Huang, J. Catal. 160 (1996) 155–170.
[38] E.C. Subbarao (Ed.), Solid Electrolytes and their Applications, Plenum Press, New York, 1980, 298 pp.
[39] R.G. Silver, C.J. Hou, J.G. Ekerdt, J. Catal. 118 (1989) 400–416.
[40] J.A. Dawson, H. Chen, I. Tanaka, Phys. Chem. Chem. Phys. 16 (2014) 4814–4822.
[41] P. Panagiotopoulou, D.I. Kondarides, Catal. Today 112 (2006) 49–52.
[42] S. Souentie, L. Lizarraga, A. Kimbolis, M. Alves-Fortunato, J.L. Valverde, P. Vernoux, J. Catal. 283 (2011) 124–132.
[43] P. Vernoux, Chem. Rev. 113 (2013) 8192–8260.
[44] M. Jacoby, Chem. Eng. News 79 (2001) 33.
[45] T. Ressler, J. Synch. Rad. 5 (1998) 118–122.
[46] G. Jacobs, L. Williams, U.M. Graham, D.E. Sparks, A. Dozier, B.H. Davis, Appl. Catal. A: Gen. 252 (2003) 107–118.
[47] K.K. Srivastava, R.N. Patil, C.B. Choudhary, K.V.G.K. Gokhale, E.C. Subbarao, Trans. Br. Ceram. Soc. 73 (1974) 85–91.
[48] B.H. Davis, J. Am. Ceram. Soc. 67 (1984) C168.
[49] R. Srinivasan, M.B. Harris, S.F. Simpson, R.J. de Angelis, B.H. Davis, J. Mater. 3 (1988) 787–797.
[50] P. Li, I.W. Chen, Phys. Rev. B 48 (1993) 10063–10071.
[51] J.E. Hahn, R.A. Scott, K.O. Hodgson, S. Doniach, S.R. Desjardins, E.I. Solomon, Chem. Phys. Lett. 88 (1982) 595–598.
[52] A.L. Roe, D.J. Scaneider, R.J. Mayer, J.W. Pyrz, J. Widson, L. Que, J. Am. Chem. Soc. 106 (1984) 1676–1681.
[53] G.E. Rush, A.V. Chadwick, J. Phys. Chem. B 104 (2000) 9597–9606.
[54] P. Li, I.W. Chen, J.E. Penner-Hahn, Phys. Rev. B 48 (1993) 10074–10081.
[55] P. He, T. Liu, A. Moslang, R. Lindau, R. Ziegler, J. Hoffmann, P. Kurinskiy, L. Common, P. Vladiminov, S.M. Nikitenko, Mat. Chem. Phys. 136 (2012) 990–998.
[56] C.M. Kalamaras, S. Americanou, A.M. Efstathiou, J. Catal. 279 (2011) 287–300.
[57] F.B. Passos, E.R. Oliveira, L.V. Mattos, F.B. Noronha, Catal. Lett. 110 (2006) 261–267.
[58] W.K. Jozwiak, React. Kinet. Catal. Lett. 30 (1986) 345–351.
[59] L.M. Acuna, D.G. Lamas, R.O. Fuentes, I.O. Fabregas, M.C.A. Fantini, A.F. Craievich, J. Rogerio, Appl. Crystal. 43 (2010) 227–236.
[60] A.V. Chadwick, M.J. Pooley, K.E. Rammutla, S.L.P. Savin, A. Rougier, J. Phys.: Condens. Matter 15 (2003) 431–440.
[61] Z. Wang, Z.Q. Chen, J. Zhu, S.J. Wang, X. Guo, Radiat. Phys. Chem. 58 (2000) 697–701.
[62] D.C. Grenoble, M.M. Estadt, D.F. Ollis, J. Catal. 67 (1981) 90–102.
[63] F.C. Meunier, A. Goguet, C. Hardacre, R. Burch, D. Thompsett, J. Catal. 252 (2007) 18–22.
[64] G. Jacobs, B.H. Davis, Int. J. Hydrogen Energy 35 (2010) 3522–3536.
[65] K.C. Petallidou, C.M. Kalamaras, A.M. Efstathiou, Catal. Today 228 (2014) 183–193.
[66] A.M. Efstathiou, K.C. Petallidou, Appl. Catal. B: Environ. 152/153 (2014) 439–443.
[67] C.M. Kalamaras, K.C. Petallidou, A.M. Efstathiou, Appl. Catal. B: Environ. 136/137 (2013) 225–238.
[68] K.C. Petallidou, K. Polychronopoulou, S. Boghosian, S. Garcia-Rodriguez, A.M. Efstathiou, J. Phys. Chem. C 117 (2013) 25467–25477.